Title
Hyperlipidemia affects multiscale structure and strength of murine femur

Journal
Journal of Biomechanics, 47(10)

ISSN
0021-9290

Authors
Ascenzi, Maria-Grazia
Lutz, Andre
Du, Xia
et al.

Publication Date
2014-07-01

DOI
10.1016/j.jbiomech.2014.04.006

Peer reviewed

Published in final edited form as:
J Biomech. 2014 July 18; 47(10): 2436–2443. doi:10.1016/j.jbiomech.2014.04.006.

Hyperlipidemia affects multiscale structure and strength of murine femur

Maria-Grazia Ascenzi[a], **Andre Lutz**[b], **Xia Du**[a], **Laureen Klimecky**[c], **Neal Kawas**[d], **Talia Hourany**[a], **Joelle Jahng**[a], **Jesse Chin**[a], **Yin Tintut**[e], **Udo Nackenhors**[f], and **Joyce Keyak**[g]

Maria-Grazia Ascenzi: mgascenzi@mednet.ucla.edu; Andre Lutz: andre.lutz@hotmail.de; Xia Du: duxia1992721@ucla.edu; Laureen Klimecky: laureen.klimecky@hotmail.fr; Neal Kawas: nealkawas@ucla.edu; Talia Hourany: talia1434@ucla.edu; Joelle Jahng: jojahng@gmail.com; Jesse Chin: jessywchin@gmail.com; Yin Tintut: ytintut@mednet.ucla.edu; Udo Nackenhors: nackenhorst@ibnm.uni-hannover.de; Joyce Keyak: jhkeyak@uci.edu

[a]Department of Orthopaedic Surgery, University of California, Los Angeles, California 90095, USA

[b]Continental Tire Company, Hannover, Germany

[c]Ostesys, 115 rue Claude Chappe, 29280 Plouzané, France

[d]Department of Molecular Oncology, John Wayne Cancer Institute, Santa Monica, California 90404, USA

[e]Department of Medicine, University of California, Los Angeles, California 90095, USA

[f]Institute of Mechanics and Computational Mechanics, Leibniz University Hannover, 30167 Hannover, Germany

[g]Department of Radiological Sciences, Medical Sciences I, Bldg 811, Room B140, University of California, Irvine, CA 92697, USA

Abstract

To improve bone strength prediction beyond limitations of assessment founded solely on the bone mineral component, we investigated the effect of hyperlipidemia, present in more than 40% of osteoporotic patients, on multiscale structure of murine bone. Our overarching purpose is to estimate bone strength accurately, to facilitate mitigating fracture morbidity and mortality in patients. Because i) orientation of collagen type I affects, independently of degree of mineralization, cortical bone's micro-structural strength; and, ii) hyperlipidemia affects collagen orientation and μCT volumetric tissue mineral density (vTMD) in murine cortical bone, we have constructed the first multiscale finite element (mFE), mouse-specific femoral model to study the effect of collagen orientation and vTMD on strength in $Ldlr^{-/-}$, a mouse model of hyperlipidemia, and its control wild type, on either high fat diet or normal diet. Each μCT scan-based mFE model included either element-specific elastic orthotropic properties calculated from collagen orientation and vTMD (collagen-density model) by experimentally validated formulation, or usual element-

Corresponding author: Maria-Grazia Ascenzi, Department of Orthopedic Surgery, Rehabilitation Bldg, Room 22-69, 1000 Veteran Avenue, University of California, Los Angeles, CA 90095, Tel. 310/825-6341, Fax 310/825-5290.

Conflict of interest statement

Dr. Ascenzi holds patents licensed to Micro-Generated Algorithms, LLC, in which she holds an interest. The other authors are without conflicts of interest.

specific elastic isotropic material properties dependent on vTMD-only (density-only model). We found that collagen orientation, assessed by circularly polarized light and confocal microscopies, and vTMD, differed among groups; and that microindentation results strongly correlate with elastic modulus of collagen-density models (r^2=0.85, $p=10^{-5}$). Collagen-density models yielded 1) larger strains, and therefore lower strength, in simulations of 3-point bending and physiological loading; and 2) higher correlation between mFE-predicted strength and 3-point bending experimental strength, than density-only models. This novel method supports ongoing translational research to achieve the as yet elusive goal of accurate bone strength prediction.

Keywords

collagen type I; multiscale finite element; high fat diet; hyperlipedimia; mouse bone

Introduction

Areal bone mineral density (aBMD) is the current clinical “gold standard” employed to diagnose patients’ osteoporosis. Such diagnosis gates opportunity for early intervention to prevent fracture. The insufficiency of low aBMD as a patient-specific facture predictor, notwithstanding its association with increased population-based fracture risk, motivated development of the FRAX index and methods that extract information from clinical imaging (Keyak et al., 1998; Boutroy et al., 2008; Li et al., 2009; Krug et al., 2010; Kazakia et al., 2011) to identify additional parameters that can aid prediction of fracture.

As a complementary path, we investigate the effect of genetic and environmental factors at the tissue level of compact bone, increasingly recognized as a major contributor of bone strength (Rockoff et al., 1969; Bonnick, 1998). We focused on factors of bone strength at tissue-level that can lead to micro-crack elongation and coalescence, and eventually to macroscopic fracture. We had previously found that changes in orientation of collagen type I, of distinct genetic and environmental origin, and reduced mineralization, can reduce cortical strength (Ascenzi et al., 2000 and 2012; Sage et al., 2011; Pirih et al., 2012). Further, collagen orientation at specific locations of the proximal tibia was found to differ in a genetic mouse model of hyperlipidemia *Ldlr*$^{-/-}$ mutant (MUT) in dependence on diet – normal diet (ND) vs. high fat diet (HFD). Recent micro-level structural analysis of the compact component of human and animal femora has established that the orientation of collagen type I (locally parallel to carbonated hydroxyapatite crystals) and the degree of calcification vary independently from each other in dependence of location, loading, and presence/absence of disease (Ascenzi, 1988; Riggs et al., 1993; Power et al., 2003; Goldman et al., 2005; Ascenzi and Lomovtsev, 2006; Ramasamya and Akkusb, 2007; Cristofolini et al., 2008; Beraudi et al., 2009 and 2010).

To predict bone strength in relation to altered parameters at bone tissue level, we present here a multiscale finite element (mFE), mouse-specific femoral model. The multiscale nature of the model enables appreciation of the effect of macroscopic mechanical testing at the bone tissue-level, to simulate experimental loading conditions *ex vivo* and *in vivo*. We apply the mFE model to femora from the hyperlipidemic MUT, its control (WT for wild

type), on either ND or HFD. Both genetic and diet-induced hyperlipidemia were previously found to increase generation of lipid oxidation that promotes bone loss and reduces bone strength (Pirih et al., 2012). Motivating this study were: i) the effect of HFD on collagen orientation of mice (Sage et al., 2011); and, ii) the hypothesis that two independent parameters, orientation of collagen and degree of calcification, affect the strength of bone in mice as they have been hypothesized to do so for humans (Ascenzi et al., 1997).

Materials and Methods

The Institutional Animal Care and Use Committee, University of California at Los Angeles, approved the experimental protocols. We used 16 right femora of 25-week-old male mice: 8 WT and 8 MUT which were for 18 weeks on either ND or HFD (TD 9022)1, Harlan Teklad), i.e. 4 groups of 4 mice per group (Pirih et al., 2012). We used μCT Skyscan 1172 (Aartselaar, Belgium) with a calibration phantom (Aartselaar, Belgium) containing two cells of 0.25 g/cm^3 and 0.75 g/cm^3 equivalent concentration of calcium hydroxyapatite, to scan the femora with isotropic voxel size of 13μm, 55kVp, 72 μA, and a 0.5 mm aluminum filter. We used the μCT axial slices (1024 × 1024 pix) and volumetric tissue mineral density (vTMD).

Mechanical testing

3-point bending was previously reported (Pirih et al, 2012). Briefly, the load was applied at femoral posterior mid-shaft, with a support span set at 6 mm, at a constant displacement rate of 6 mm/min to total failure. Thereafter, we performed 4 microindentations per femur (3 femora per group), starting above the complete transverse fracture at mid-shaft, every 1 to 2 mm at anterior quadrant, towards proximal end, with BioDent 1000 RPI (Active Life Scientific). With one probe fixed at the bone surface, the moving probe cyclically indented the tissue relative to bone surface. The pre-load of the reference probe was 2.7 N ± 0.25 N for all measurements. A BP1 probe (25 μm tip radius with a 90° conical end) was used with 2 N force, 20 cycles of indentation per measurement, 2 Hz, for all indentations. So-called average unloading slope (Avg US (1st-L), N/μm) provides the average unloading slopes of each measurement, from 1st to Last (Randall et al., 2009).

Microscopy

We used circularly polarized light (CPL) microscopy to visualize birefringent signals indicative of collagen orientation (Ascenzi and Lomovtsev, 2006), and scanning confocal microscopy to visualize actual collagen orientation in the cortical component of the femoral shaft. 50μm thick serial anterior-posterior longitudinal sections of the shaft embedded in PMMA were observed at 100× with a Leitz Dialux 20 microscope with CPL (Midland, Ontario, Canada) (Ascenzi et al., 2012). A Leica TCS-SP (Wetzlar, Germany) microscope with krypton laser (567 nm excitation), 20× and 63× Planapochromat lens, 580–700 nm detection range allowed observation of CPL birefringent extinct and bright locations at 200×. CPL and confocal images were analyzed with XaraX (Xara Group Ltd) and Metamorph (Molecular Devices) software. In particular, we compared corresponding locations between microindented femora (3 per group) and non-microindented femora (1 per group). For each quadrant, we combined the data within 1mm bins along the z-axis, and

computed the percentage of bright area with respect to total area. Bright birefringence observed on longitudinal sections was set to correspond to an 64% of longitudinal (0° ±22.5°), 19% of oblique acute (45°±22.5°), 3% of transverse (90°±22.5°), and 14% of oblique obtuse orientation (135°±22.5°) of collagen; and complement extinct birefringence set to correspond to 4% of longitudinal, 29% of oblique acute, 34% of transverse, and 33% of oblique obtuse orientation of collagen (Ascenzi and Lomovtsev, 2006).

Two-level mFE model

For each of the 16 femora, the macro-geometry of the mFE model was obtained from the quantitative μCT, and meshed with tetrahedral elements (~ 115,000) with mean edge size of 0.17 mm (Lutz and Nackenhorst, 2010). An element was considered bone, not marrow, if its calcium hydroxyapatite density was at least 0.5 g/cm^3. We choose an xyz reference with x-axis directed from medial to lateral aspect, y-axis from anterior to posterior, z-axis from distal to proximal along the long axis of shaft.

We prepared 16 so-called collagen-density models whose simulated cortical component consisted of element-specific elastic orthotropic properties calculated from collagen orientation and vTMD, (see entries [1,1] to [6,6], Appendix A). These orthotropic properties follow the observation that murine cortical bone consists mainly of lamellar bone (Bianco and Robey, 2000). Indeed, we modeled the micro-structure as a locally unidirectional fiber composite (Vinson, 1993), where the collagen fibrils represent the composite's matrix and the apatite crystallites represent the fibers. Because collagen and apatite form lamellar bone of both human secondary osteons and mouse bone, we used a lamellar model verified by mechanical testing of single extinct or bright osteons at initial and final degrees of calcification: we extended formulae previously developed to simulate prestress in single fully calcified lamellae and mechanical testing of single human fully-calcified osteons. We wrote an algorithm to distribute the element-specific assignment of collagen orientation so as to respect the percentages of longitudinal, oblique acute, transverse and oblique obtuse orientations of each quadrant and bin. The algorithm chooses randomly among such percentages with the restriction of a smaller than 10° change between orientations in adjacent elements (Ascenzi and Lomovtsev, 2006; Ascenzi et al., 2008). We also prepared 16 so-called density-only models with element-specific elastic isotropic properties computed from μCT vTMD (Lutz and Nackenhorst, 2010). We computed the Young's modulus

$$E = E_o(\rho/\rho_o)^2 \quad (1)$$

with E_o = 6250 MPa, ρ_o=2 g/cm^3, ρ as vTMD. The Poisson's ratio was 0.29.

We simulated 3-point bending and physiological loading (Fig. 1) producing strains in the same elastic range. For the 3-point bending, we calculated bone strength (defined as load at yield point) from load-displacement diagrams, as load at 90% of maximum load (Cody et al. 1996). We used the yield point to ensure that models' load and displacement fell within the elastic range. A force of 3N, directed along the negative direction of the y-axis, was applied as node displacement of an element face. We checked that the force applied to the model produced a stress/strain ratio comparable to the elastic modulus in each specific principal direction. To simulate physiological loading in terms of one hind-legged stance, a force of

4N, forming a 20° angle with the z-axis and parallel to the projection of the femoral neck axis on the xy-plane (Keyak et al, 1998; Voide, 2008), was applied over a 0.35 μm-diameter region of the femoral head as node displacement. We fully restrained the nodes at the distal end. We analyzed the mFE models with Abaqus software (Dassault Systèmes) on UCLA's Hoffman cluster and UCSD's Trestles supercomputer. The 20MB file size was due to the highly heterogeneous element-specific material properties. The 10 hours of computing time used 8 cores and 48 GB of RAM.

We investigated strain along the femoral shaft, $\boldsymbol{\varepsilon}_{zz}$, at the region of highest absolute value, i.e. at anterior and posterior quadrants of mid-shaft. Because the average diameter of mid-shaft is the same for all femora except for a significant difference between ND MUT and HFD MUT (1.78±0.02 mm vs. 1.62±0.03 mm, $p<0.01$), we adjusted the computed $\boldsymbol{\varepsilon}_{zz}$ for HFD MUT with respect to the ND MUT (Appendix B). Afterwards, we computed the mFE-predicted strength for 3-point bending by noting that the mFE model behaves linearly and by assuming that yielding begins when the maximum longitudinal strain at the mid-shaft of the mFE model, $\boldsymbol{\varepsilon}_{zz}$, is 0.6% (Morgan and Keaveny, 2001; Kaneko et al., 2003). Therefore, mFE-predicted strength was computed as $0.006*(3/\varepsilon_{zz})$, where 3 (N) is the magnitude of the force applied. Accordingly, higher surface strain ε_{zz} corresponds to lower strength. We then examined the correlation between the measured bone strength and mFE-predicted strength. Analogous to the use of ε_{zz} at the bone surface to compute the mFE-predicted bone strength for 3-point bending simulations, we studied the average ε_{zz} at the bone surface in the physiological loading simulations to infer changes in bone strength among mouse groups.

Statistical analysis

We used the Student t-tests to detect differences of $\boldsymbol{\varepsilon}_{zz}$ between collagen-density and density-only models of each mouse group (4 mice per group); and among the 4 mouse groups for collagen-density and density-only models, separately. We used the r^2 as measure of correlation, and the p-value of the r^2 with a t-test of slopes between linear regression and horizontal line, between Avg US (1st-L) and mFE elastic modulus at microindentation site for 48 microindentations, and between experimental strength and mFE-predicted strength of 16 femora. The p-value of single comparisons was considered significant if smaller than 0.05, of m multiple comparisons if smaller than Bonferroni's 0.05/m, for m. The data are presented as mean ± standard error.

Results

We identified and quantified the effect of murine hyperlipidemia on the multiscale structural properties of the femur, assessed strain with mFE femoral models, and studied the relation between experimental and mFE strength.

At the micro-structural level, the distribution of % birefringent bright area and collagen orientation showed no difference from mid-shaft to proximal femur (bins 1 through 7) and from mid-shaft to distal femur (bins 8 through 14). Hence the data are presented per mouse group for bins 1 to 7. The % birefringent bright area was found to be 1) largest at the anterior quadrant and overall smallest at the posterior quadrant of WT femur (on ND or HFD); 2) increased in all the quadrants from mid-shaft to proximal femur of ND MUT; and

3) smallest at anterior and lateral quadrants, and largest at posterior and medial quadrants, c onsistently from mid-shaft to proximal femur of HFD MUT (Figs. 2, 3a, 3b). The collagen orientation was predominantly longitudinal at 1) anterior quadrant of WT (on ND or HFD); 2) all quadrants of proximal femur of ND MUT; and 3) posterior and medial quadrants of HFD MUT (Table I, Figs. 3c, 3d).

vTMD, averaged over the femoral bone, differed among mouse groups: ND WT: 1.59±0.001 g/cm^3; HFD WT: 1.51±0.001 g/cm^3; ND MUT: 1.54±0.001 g/cm^3; HFD MUT: 1.45±0.001 g/cm^3; $p<10^{-25}$. Avg US (1st-L) from microindentation differs between ND MUT and HFD MUT (0.49±0.03 N/μm vs. 0.36±0.02 N/μm; p=0.02). The correlation between Avg US (1st-L) measured with indentation tip penetrating along the anterior-posterior (y) axis (Fig.1), and the elastic modulus computed from both collagen orientation and vTMD along the y-axis was stronger for the collagen-density models than the density-only models (r^2=0.85, $p=10^{-5}$; vs. r^2=0.42, p=0.007; Fig. 4).

For both loading conditions, $\boldsymbol{\varepsilon}_{zz}$ was 1) predominantly positive at anterior, suggesting tension along the femoral z-axis; and predominantly negative at posterior quadrant, suggesting compression along the femoral z-axis (Table II); and 2) predominantly larger in magnitude for collagen-density models than density-only models (Table II). For 3-point bending, 1) $\boldsymbol{\varepsilon}_{zz}$ was significantly larger for collagen-density than density-only models at the anterior quadrant of ND WT, HFD WT, and ND MUT (Table II, Fig. 5); 2) neither collagen-density nor density-only models found significant differences in ε_{zz} among mouse groups (Table III and Supplemental Table; note that significant differences in #1 of Table III are listed as non significant in Supplemental Table after strain adjustment of HFD MUT); 3) the predominantly larger $\boldsymbol{\varepsilon}_{zz}$ for the collagen-density models yielded lower mFE-predicted strength than the density-only models (Fig. 6); and 4) the correlations between experimental strength and mFE-predicted strength, computed for ND WT, HFD WT and ND MUT at the anterior quadrant, for which $\boldsymbol{\varepsilon}_{zz}$ significantly differed between collagen-density and density-only models (Table II), was stronger for the collagen-density than the density-only models (r^2=0.91, $p=5\times10^{-4}$; vs. 0.73; $p=2\times10^{-6}$). For physiological loading, 1) in the posterior quadrant, ε_{zz} was significantly larger in magnitude for collagen-density models than for density-only models, with differences occurring in the ND WT, HFD WT, and HFD MUT groups; 2) in the anterior quadrant, collagen-density models revealed one significant difference in ε_{zz} among the mouse groups, compared with two differences the density-only models revealed two (Fig. 7); and 3) in the posterior quadrant, collagen-density models demonstrated five significant differences compared with three for the density-only models. To study the implications of such differences on bone strength, we looked at the magnitude of εzz at the bone surface. At the posterior surface, the magnitude of εzz significantly differed between ND WT and HFD WT, and between HFD WT and ND MUT, for density-only models (ND WT: 289 ± 24 vs. HFD WT: 618 ± 25 vs. ND MUT: 387 ± 20; p<0.0005), but not for collagen-density models (ND WT: 469 ±49 vs. HFD WT: 743 ± 98 vs. ND MUT: 386 ± 40; p>0.0277; p is significant if less than 0.0083). Therefore, we infer that the distribution of collagen orientation, that is unchanged by the HFD in WT and is changed by the genetic mutation in ND MUT, compensates for the lower vTMD of the HFD WT, to yield unchanged bone strength among ND WT, HFD WT and ND MUT.

Discussion

We have developed a new methodology to assess mouse-specific bone strength for investigations on the effect of genetic and environment on bone quality. We have made the first application to a mouse model of genetic hyperlipidemia with diet as environmental factor.

Epidemiological studies associate hyperlipidemia with low bone mass (Adami et al., 2004; Orozco et al., 2004; Cui et al., 2005). HFD-induced hyperlipidemia reduces bone formation, mineral density and strength in animal studies (Parhami et al., 2001; Turek et al., 2003; Pirih et al. 2012). Hyperlipidemia 1) increases lipid oxidation products that blunt osteoblastic function; and 2) induces osteoclastic differentiation (Greenfield et al., 1993; Parhami et al., 1997; Huang et al., 2007; Hirasawa et al., 2007). In the present study, we found that hyperlipidemic MUT mice, either on a ND or HFD, had altered collagen orientation in long bones. Recent studies also show that lipid oxidation products reduce the anabolic effect of parathyroid hormone PTH(1–34) treatment of osteoporosis (Huang et al., 2007; Sage et al., 2011). One of the beneficial effects of PTH(1–34) treatment includes increased heterogeneity of collagen orientation in osteoporotic patients (Ascenzi et al., 2012), but the present study suggests that hyperlipidemia may also impair PTH(1–34) effects on collagen orientation. Further, because the HFD is also diabetogenic, Pirih et al. (2012) conjectured occurrence of insulin resistance with subsequent induction of advanced glycation end-products, and hypothesized additional involvement of non-canonical pathways of osteoclastogenesis, such as through TNF-a and IGF-I, and of factors affecting osteoprogenitors.

Our results on the ND WT indicate prevalent orientation forming small angle with the longitudinal axis of the femur at anterior quadrant and larger angles with the longitudinal axis of the femur at posterior quadrant, confirming previous findings (Ramasamya and Akkusb, 2007). Also, the effect of HFD on MUT's collagen orientation, now quantified in the cortical component of the whole shaft, confirms that the HFD alters the orientation of collagen in the MUT (Sage et al., 2011). Over the last fifty years, the experimental findings on the orientation of collagen type I have given rise to models of orientation patterns, that were incorporated in models to analyze the effect of such orientation (for reviews, Ascenzi et al., 1999, 2008 and 2013). Interestingly, we found that the distribution of collagen orientation does not differ between upper and lower shaft of murine femur. This contrasts with the difference found in the human femur (Ascenzi, 1988), perhaps due to presence and location-dependent size variation of secondary osteons (Evans, 1973) interacting with the variation of collagen orientation along the shaft to strengthen the shaft of human long bones, in addition to the load distribution difference between bipeds and quadrupeds.

The higher ε_{zz} found in the collagen-density models, in comparison to the density-only models, indicates that the strain on osteocytes is higher th an anticipated. Our higher strain increases the possibility that such cells are indeed able to sense the strain exerted by the surrounding bone matrix and signal for bone remodeling (Bonewald, 2011). Further, we found that one of the parameters measured by the BioDent RPI instrument, the average unloading slope Avg US (1st-L), was well predicted by the elastic modulus in the direction

of microindentation penetration. We interpret this result in light of the parallelism of orientation between collagen and hydroxyapatite needles (Bonucci, 2000) that would pose a different resistance to the microindenter, as previously hypothesized in regard to nanoindentation (Reisinger et al, 2011).

Murine finite element models usually used to study bone defects are based on μCT vTMD, here called density-only models (Spatz et al., 2013). Because the organization of collagen type I orientation in murine long bone was previously found to depend on genetic and environmental factors (Ramasamya and Akkusb, 2007; Ionova-Martin et al., 2010; Tang et al., 2012), we tested whether the mechanical performance of bone with altered patterns would show reduced strength. To this end, we newly developed a collagen-density mFE femoral model, and compared the new model to usual density-only models. When we adjusted the micro-level stress for bone diameter at mid-shaft of group HFD MUT, we employed a scaling factor for continuum-level stress in a homogeneous isotropic hollow cylinder subjected to bending. This allowed us to correct only for differences in bone diameter without considering material differences. We then used the compliance matrix for the orthotropic heterogeneous micro-structure to compute the adjusted micro-level strain. This approach assumes that the effect of bone diameter on micro-level stress is proportional to that on continuum-level stress, which is reasonable for this comparative study. Nevertheless, this is a limitation of the study.

Strain ε_{zz} at the femoral mid-shaft differs between loading conditions, between collagen-density and density-only models, and among mouse groups. The different ε_{zz} between loading conditions confirms that the macro-geometry affects physiological loading's ε_{zz} even though femoral neck angles do not differ significantly among the mouse groups. The difference in results between collagen-density and density-only models, at anterior and posterior quadrants (Table III), shows that the effect of collagen orientation is quadrant-dependent. Because the difference in ε_{zz} between ND WT and HFD WT of density-only models, is missing in collagen-density models, collagen orientation appears to compensate for difference in vTMD (Table III, #2). Collagen orientation also has a differentiating effect on ε_{zz} between HFD MUT and each of ND WT and ND MUT, which is missing in density-only models (Table III, #3). Further, differences in mean and standard error of vTMD affect ε_{zz}: vTMD is greater in HFD MUT vs. ND MUT at specific locations within the anterior mid-shaft. We find that the investigated genetic mutation affects the distribution of collagen orientation, but diet affects collagen orientation only in conjunction with the genetic mutation. The unchanged collagen orientation of the HFD WT compensates for its lower vTMD compared with that of ND MUT, to yield the same bone strength of the ND MUT despite a less than optimal collagen orientation. The lack of additional differences in bone strength among the mouse groups is due to the fact that the femur does not break at mid-shaft under physiological loading. The present work provides foundation for further studies on the implications of diet and genetics for organization of elementary components and bone strength at locations of fracture occurrence in humans, even though the mouse groups considered do not fracture.

Our new mFE model uses animal-specific findings. Namely, animal-specific observations of collagen direction supplement the μCT grey values (interpreted as hydroxyapatite), and

water is included indirectly through validation of mechanical testing of wet micro-specimens. Including collagen orientation in the elastic mFE model increases the Young's modulus in the direction of collagen and slightly reduces the Young's modulus in the two perpendicular directions, to yield an average Young's modulus on the order of the isotropic Young's modulus of the density-only models. For instance, because the majority of collagen forms small a ngles with the longitudinal axis of the femur at the anterior quadrant of the ND WT, and forms large angles with the longitudinal axis of the femur at the posterior quadrant, the strain component ε_{zz} is larger at the anterior quadrant in collagen-density models in comparison to density-only models, and smaller at the posterior quadrant in collagen-density models in comparison to density-only models (Table II). Recently Blanchard et al. (2013) differently interpreted the μCT grey shade, considering it a fixed combination of densities of collagen, hydroxyapatite and water, where collagen and water would attenuate the grey shade. Their models, incorporating a fixed (generic, not animal-specific) orientation of mineralized collagen, to reinforce the transversely isotropic material properties, yield smaller strains than usual density-only models.

Our novel approach advances the field by identifying and quantifying the effect of specific genetic and environmental factors on multiscale structural parameters of mouse-specific bone quality. Inclusion of both collagen orientation and mineralization in the mFE models, instead of including only mineralization, improves predictions of bone strength. We provide a foundation for translational research to achieve bone strength prediction from patient-specific genetic and environmental factors, with a view to preventive treatment.

Supplementary Material

Refer to Web version on PubMed Central for supplementary material.

Acknowledgments

This research was supported by XSEDE (NSF grant # OCI-1053575), UCLA's Hoffman2 Cluster; and Orthopedic Hospital Research Center. The authors thank Active Life Scientific for microindentation, Alexandre Lomovtsev for image preparation, Josh Kimmel for manuscript preparation, and Mahidas Tatenani (XSEDE Extended Collaborative Support Service) and Tajendra Singh (UCLA's Institute for Digital Research) for computing assistance.

References

Adami S, Braga V, Zamboni M, Gatti D, Rossini M, Bakri J, Battaglia E. Relationship between lipids and bone mass in 2 cohorts of healthy women and men. Calcified Tissue International. 2004; 74:136–142. [PubMed: 14668965]

Ascenzi A. The micromechanics versus the macromechanics of cortical bone - a comprehensive presentation. Journal of Biomechanical Engineering. 1988; 110:357–363. [PubMed: 3060679]

Ascenzi A, Ascenzi M-G, Benvenuti A, Mango F. Pinching in longitudinal and alternate osteons during cyclic loading. Journal of Biomechanics. 1997; 30:689–695. [PubMed: 9239548]

Ascenzi A, Bonucci E. The tensile properties of single osteons. The Anatomical Record. 1967; 158:375–386. [PubMed: 4861577]

Ascenzi A, Bonucci E. The compressive properties of single osteons. The Anatomical Record. 1968; 161:377–391. [PubMed: 4879362]

Ascenzi A, Bonucci E. The shearing properties of single osteons. The Anatomical Record. 1972; 172:499–510. [PubMed: 5011944]

Ascenzi A, Bonucci E. Relationship between ultrastructure and "pin test" in osteons. Clinical Orthopaedics and Related Research. 1976; 121:275–294. [PubMed: 991513]

Ascenzi M-G, Gill J, Lomovtsev A. Collagen orientation patterns around osteocyte lacunae in human secondary osteons by confocal microscopy. Journal of Biomechanics. 2008; 41:3428–3437.

Ascenzi M-G. A first estimation of prestress in so-called circularly fibered osteonic lamellae. Journal of Biomechanics. 1999; 32:935–942. [PubMed: 10460130]

Ascenzi, M-G.; Benvenuti, A.; Ascenzi, A. Single osteon micromechanical testing. In: An, Y.; Draughn, R., editors. Mechanical Testing of Bone. Boca Raton, Florida: CRC Press; 2000. p. 271-290.

Ascenzi, M-G.; Kawas, N.; Lutz, A.; Kardas, D.; Nackenhorst, U.; Keyak, J. Individual-specific, multi-scale finite element simulation of the proximal femur cortex. In: Ching-Long, L., editor. Journal of Computational Physics. 2013. p. 298-311.of special issue on Multi-scale Modeling 244

Ascenzi M-G, Liao VP, Lee BM, Billi F, Zhou H, Lindsay R, Cosman F, Nieves J, Bilezikian JP, Dempster DW. Parathyroid hormone treatment improves the cortical bone microstructure by improving the distribution of type I collagen in postmenopausal women with osteoporosis. Journal of Bone Mineral Research. 2012; 27:702–712. [PubMed: 22161803]

Ascenzi M-G, Lomovtsev A. Collagen orientation patterns in human secondary osteons, quantified in the radial direction by confocal microscopy. Journal of Structural Biology. 2006; 153:14–30. [PubMed: 16399238]

Beraudi A, Stea S, Bordini B, Baleani M, Viceconti M. Collagen orientation in human femur, tibia and fibula shaft by circularly polarized light. Bone. 2009; 44:S320.

Beraudi A, Stea S, Bordini B, Baleani M, Viceconti M. Osteon classification in human fibular shaft by circularly polarized light. Cells Tissues Organs. 2010; 191:260–268. [PubMed: 19776542]

Bianco P, Robey PG. Marrow stromal stem cells. Journal of Clinical Investigation. 2000; 105:1663–1668. [PubMed: 10862779]

Blanchard R, Dejaco A, Bongaers E, Hellmich C. Intravoxel bone micromechanics for micro CT-based finite element simulations. Journal of Biomechanics. 2013; 46:2710–2721. [PubMed: 24016680]

Bonewald LF. The amazing osteocyte. Journal of Bone and Mineral Research. 2011; 26:229–238. [PubMed: 21254230]

Bonnick, SL. Skeletal anatomy in densitometry. In: Bonnick, SL., editor. Bone Densitometry in Clinical Practice. New York, NY: Humana Press; 1998. p. 35-78.

Bonucci, E. Basic composition and structure of bone. In: An, Y.; Draughn, R., editors. Mechanical Testing of Bone. Boca Raton, Florida: CRC Press; 2000. p. 3-22.

Boutroy S, Van Rietbergen B, Sornay-Rendu E, Munoz F, Bouxsein ML, Delmas P. Finite element analysis based on in vivo HR-pQCT images of the distal radius is associated with wrist fracture in postmenopausal women. Journal of Bone Mineral Research. 2008; 23:392–399. [PubMed: 17997712]

Cody DC, McCubbrey DA, Divine GW, Gross GJ, Goldstein SA. Predictive value of proximal femoral bone densitometry in determining local orthogonal material properties. Journal of Biomechanics. 1996; 29:753–761. [PubMed: 9147972]

Cristofolini L, Taddei F, Baleani M, Baruffaldi F, Stea S, Viceconti M. Multiscale investigation of the functional properties of the human femur. Philosophical Transactions of the Royal Society A: Mathematical, Physical and Engineering Sciences. 2008; 366:3319–3341.

Cui LH, Shin MH, Chung EK, Lee YH, Kweon SS, Park KS, Choi JS. Association between bone mineral densities and serum lipid profiles of pre- and post-menopausal rural women in South Korea. Osteoporosis International. 2005; 16:1975–1981. [PubMed: 16167087]

Evans, FG. Mechanical properties of bone. Springfield, Illinois: Thomas Publisher; 1973. p. 282-310.

Goldman HM, Thomas CD, Clement JG, Bromage TG. Relationships among microstructural properties of bone at the human midshaft femur. Journal of Anatomy. 2005; 206:127–139. [PubMed: 15730478]

Greenfield EM, Gornik SA, Horowitz MC, Donahue HJ, Shaw SM. Regulation of cytokine expression in osteoblasts by parathyroid hormone: rapid stimulation of interleukin-6 and leukemia inhibitory factor mRNA. Journal of Bone and Mineral Research. 1993; 8:1163–1171. [PubMed: 8256653]

Hirasawa H, Tanaka S, Sakai A, Tsutsui M, Shimokawa H, Miyata H, Moriwaki S, Niida S, Ito M, Nakamura T. ApoE gene deficiency enhances the reduction of bone formation induced by a high-fat diet through the stimulation of p53-mediated apoptosis in osteoblastic cells. Journal of Bone and Mineral Research. 2007; 22:1020–1030. [PubMed: 17388726]

Huang MS, Morony S, Lu J, Zhang Z, Bezouglaia O, Tseng W, Tetradis S, Demer LL, Tintut Y. Atherogenic phospholipids attenuate osteogenic signaling by BMP-2 and parathyroid hormone in osteoblasts. Journal of Biological Chemistry. 2007; 282:21237–21243. [PubMed: 17522049]

Ionova-Martin SS, Do SH, Barth HD, Szadkowska M, Porter E, Ager JW III, Ager JW Jr, Alliston T, Vaisse C, Ritchie RO. Reduced size-independent mechanical properties of cortical bone in high-fat diet-induced obesity. Bone. 2010; 46:217–225. [PubMed: 19853069]

Kaneko TS, Pejcic MR, Tehranzadeh, Keyak JH. Relationships between material properties and CT scan data of cortical bone with and without metastatic lesions. Medical Engineering & Physics. 2003; 25:445–454. [PubMed: 12787982]

Kazakia GJ, Burghardt AJ, Link TM, Majumdar S. Variations in morphological and biomechanical indices at the distal radius in subjects with identical BMD. Journal of Biomechanics. 2011; 44:257–266. [PubMed: 21071031]

Keyak JH, Rossi SA, Jones KA, Skinner HB. Prediction of femoral fracture load using automated finite element modeling. Journal of Biomechanics. 1998; 31:125–133. [PubMed: 9593205]

Krug R, Burghardt AJ, Majumdar S, Link TM. High-resolution imaging techniques for the assessment of osteoporosis. Radiologic Clinics of North America. 2010; 48:601–621. [PubMed: 20609895]

Li W, Kornak J, Harris T, Keyak J, Li C, Lu Y, Cheng X, Lang T. Identify fracture-critical regions inside the proximal femur using statistical parametric mapping. Bone. 2009; 44:596–602. [PubMed: 19130910]

Lutz A, Nackenhorst U. Numerical investigations on the biomechanical compatibility of hip-joint endoprostheses. Archive of Applied Mechanics. 2010; 80:503–512.

Morgan EF, Keaveny TM. Dependence of yield strain of human trabecular bone on anatomic site. Journal of Biomechanics. 2001; 34:569–577. [PubMed: 11311697]

Orozco P. Atherogenic lipid profile and elevated lipoprotein (a) are associated with lower bone mineral density in early postmenopausal overweight women. European Journal of Epidemiology. 2004; 19:1105–1112. [PubMed: 15678790]

Parhami F, Morrow AD, Balucan J, Leitinger N, Watson AD, Tintut Y, Berliner JA, Demer LL. Lipid oxidation products have opposite effects on calcifying vascular cell and bone cell differentiation. A possible explanation for the paradox of arterial calcification in osteoporotic patients. Arterioscler Thromb Vasc Biol. 1997; 17:680–687. [PubMed: 9108780]

Parhami F, Tintut Y, Beamer WG, Gharavi N, Goodman W, Demer LL. Atherogenic high-fat diet reduces bone mineralization in mice. Journal of Bone and Mineral Research. 2001; 16:182–188. [PubMed: 11149483]

Pirih F, Lu J, Ye F, Bezouglaia O, Atti E, Ascenzi M-G, Tetradis S, Demer L, Aghaloo T, Tintut Y. Adverse effects of hyperlipidemia on bone regeneration and strength. Journal of Bone Mineral Research. 2012; 27:309–318. [PubMed: 21987408]

Power J, Loveridge N, Lyon A, Rushton N, Parker M, Reeve J. Bone remodeling at the endocortical surface of the human femoral neck: a mechanism for regional cortical thinning in cases of hip fracture. Journal Bone Mineral Research. 2003; 18:1775–1780.

Ramasamya JG, Akkusb O. Local variations in the micromechanical properties of mouse femur: The involvement of collagen fiber orientation and mineralization. Journal of Biomechics. 2007; 40:910–918.

Randall C, Mathews P, Yurtsev E, Sahar N, Kohn D, Hansma P. The bone diagnostic instrument III: Testing mouse femora. Review of Scientific Instruments. 2009; 80:065108–065108. [PubMed: 19566227]

Reisinger AG, Pahr DH, Zysset PK. Elastic anisotropy of bone lamellae as a function of fibril orientation pattern. Biomechanical Models in Mechanobiology. 2011; 10:67–77.

Reznikov N, Almany-Magal R, Shahar R, Weiner S. Three-dimensional imaging of collagen fibril organization in rat circumferential lamellar bone using a dual beam electron microscope reveals ordered and disordered sub-lamellar structures. Bone. 2013; 52:676–683. [PubMed: 23153959]

Riggs CM, Vaughan LC, Evans GP, Lanyon LE, Boyde A. Mechanical implications of collagen fibre orientation in cortical bone of the equine radius. Anatomy and Embryology. 1993; 187:239–248. [PubMed: 8470824]

Rockoff SD, Sweet E, Bleustein J. The relative contribution of trabecular and cortical bone to the strength of human lumbar vertebrae. Calcified Tissue Research. 1969; 3:163–175. [PubMed: 5769902]

Sage AP, Lu J, Atti E, Tetradis S, Ascenzi M-G, Adams DJ, Demer LL, Tintut Y. Hyperlipidemia induces resistance to PTH bone anabolism in mice via oxidized lipids. Journal of Bone Mineral Research. 2011; 26:1197–1206. [PubMed: 21611962]

Spatz JM, Ellman R, Cloutier AM, Louis L, van Vliet M, Suva LJ, Dwyer D, Stolina M, Ke HZ, Bouxsein ML. Sclerostin antibody inhibits skeletal deterioration due to reduced mechanical loading. Journal of Bone and Mineral Research. 2013; 28:865–874. [PubMed: 23109229]

Tang SY, Herber RP, Ho SP, Alliston T. Matrix metalloproteinase-13 is required for osteocytic perilacunar remodeling and maintains bone fracture resistance. Journal of Bone and Mineral Research. 2012; 27:1936–1950. [PubMed: 22549931]

Turek JJ, Watkins BA, Schoenlein IA, Allen KG, Hayek MG, Aldrich CG. Oxidized lipid depresses canine growth, immune function, and bone formation. Journal of Nutritional Biochemistry. 2003; 14:24–31. [PubMed: 12559474]

Vinson, JR. The behavior of shells composed of isotropic and composite materials. Dordrecht: Kluwer Academic Publishers; 1993. p. 286-320.

Voide R, van Lenthe GH, Müller R. Femoral stiffness and strength critically depend on loading angle: a parametric study in a mouse-inbred strain. Biomedizinische Technik. 2008; 53:122–129. [PubMed: 18601620]

Appendix A

The material properties at bone-tissue level were modeled as a locally unidirectional fiber composite (Ascenzi, 1999), where the collagen fibrils represented the composite's matrix, and the carbonated apatite crystallites represented the fibers. The stiffness matrix relative to a specific collagen orientation followed the composite formulation with small displacements (Vinson, 1993) and used vTMD from μCT for the apatite contained in the elements (Ascenzi, 1999). We used Maple software and Python 1.3 for property assignment to element. First, a stiffness matrix Q_h for the linear orthotropic material with respect to the longitudinal axis of the femur, was written in terms of the nine variables that define such material. Then values of the variables determined by elastic moduli, shear moduli and Poisson's ratios previously obtained through mechanical testing, were specified. Specifically, 11.6 GPa and 5.5 GPa were used for the respective longitudinal and transverse elastic moduli for extinct birefringence, and 6.3 GPa was used for the longitudinal and transverse elastic moduli. 4 GPa was assigned to the shear modulus and 0.3 to the Poisson's ratio (Ascenzi and Lomovtsev, 2006; Ascenzi and Bonucci, 1967, 1968, 1972, 1976; Ascenzi et al., 1997; Bonucci, 2000).

Second, a stiffness matrix Q_f that represents the locally unidirectionally-fibered material, transversely isotropic along the circumferential (axis 2) and longitudinal (axis 3) directions, was written in terms of five parameters, of which three were known (Ascenzi, 1999). The unknown parameters of Q_h and of Q_f were then obtained by solving the system of equations resulting by equating the orthotropic matrix Q_h with the matrix that averages radially the contributions of the conjugate matrices $(T_\gamma)^{-1}Q_f\ T_\gamma$, where $T\gamma$ is the rotation matrix around the radial axis 1 relative to the collagen orientation defined by the angle γ (Vinson, 1993). By so doing, the material properties assigned to the elements of the mFE model by means of

the matrix $(T_\gamma)^{-1}Q_f\ T_\gamma$, in combination, yield overall the homogeneous material properties experimentally observed for single osteons. Here *d* = element-specific vTMD, *co* = element-specific collagen orientation with respect to the z-axis within the circumferential-axial reference. The 21 [i,j] entries of the symmetric matrix $(T_\gamma)^{-1}Q_f\ T_\gamma$ are:

```
[1,1]=10^5*(4.17*d^2+88.57*d+470.01)/(477.00*d+4928.00);
[1,2]=10^5*(1.68*d^2-0.25*d*cos(0.017*co)^2*d+35.71*d-2.53*d*cos(0.017*x)^2-
2.72*cos(0.017*co)^2*d+189.66-27.47*cos(0.017*co)^2)/(477.00*d+4928.00);
[1,3]=10^6*(1.10*d^2-1.65*cos(0.017*co)^2*d^2+0.97*cos(0.017*co)^4*d^2+22.89*
d-
31.86*cos(0.017*co)^2*d+17.83*cos(0.017*co)^4*d+118.81-
152.77*cos(0.017*co)^2+80.96*cos(0.017*co)^4)/(477.00*d+4928.00);
[1,4]=10^5*(0.25*d*cos(0.017*co)^2*d+2.53*d*cos(0.017*co)^2*d
+2.53*cos(0.017*co)^2*d+
1.43*d^2+30.47*d+2.72*cos(0.017*co)^2*d+27.47*cos(0.017*co)^2+
162.19)/(477.00*d+4928.00);
[1,5]=10^5*(9.67*cos(0.017*co)^2*d^2-9.67*cos(0.017*co)^4*d^2+178.30*cos(0.01
7*co)^2*d-
178.30*cos(0.017*co)^4*d+1.68*d^2+35.71*d+809.64*cos(0.017*co)^2-
809.64*cos(0.017*co)^4+189.66)/(477.00*d+4928.00);
[1,6]=10^5*(9.67*cos(0.017*co)^4*d^2+178.30*cos(0.017*co)^4*d-2.82*cos(0.017*
co)^2*d^2-
37.96*cos(0.017*co)^2+809.64*cos(0.017*co)^4-91.54*cos(0.017*co)^2+
4.17*d^2+88.57*d+470.01)/(477.00*d+4928.00);
[2,2]=10^5*(0.25*sin(0.017*co)*cos(0.017*co)*d^2+
5.24*sin(0.017*co)*cos(0.017*co)*d+
27.47*sin(0.017*co)*cos(0.017*co))/(477.00*d+4928.00);
[2,3]=10^5*(8.26*sin(0.017*co)*cos(0.017*co)*d^2-9.67*sin(0.017*co)*cos(0.017
*co)^3*d^2+
159.31*sin(0.017*co)*cos(0.017*co)*d-178.30*sin(0.017*co)*cos(0.017*co)^3*d+
763.87*sin(0.017*co)*cos(0.017*co)-809.64*sin(0.017*co)*cos(0.017*co)^3)/
(477.00*d+4928.00);
[2,4]=10^5*(9.67*sin(0.017*co)*cos(0.017*co)^3*d^2+178.30*sin(0.017*co)*cos(0
.017*co)^3*d+
809.64*sin(0.017*co)*cos(0.017*co)^3-1.41*sin(0.017*co)*cos(0.017*co)*d^2-
18.98*sin(0.017*co)*cos(0.017*co)*d-45.77*sin(0.017*co)*cos(0.017*co))/
(477.00*d+4928.00);
[2,5]=10^6*(1.93*cos(0.017*co)^2*d^2-1.93*cos(0.017*co)^4*d^2+35.66*d*cos(0.0
17*co)^2-
35.66*cos(0.017*co)^4*d
+161.93*cos(0.017*co)^2-161.93*cos(0.017*co)^4+0.11*d^2+
3.39*d+23.46)/(477.00*d+4928.00);
[2,6]=0; [3,3]=0; [3,4]=0; [3,5]=0;
[3,6]=10^2*(2.87*d-0.61*cos(0.017*co)^2*d+31.23+16.37*cos(0.017*co)^2);
```

```
[4,4]=0; [4,5]=0; [4,6]=0; [5,5]=0;
[5,6]=10^2*(-0.61*sin(0.017*co)*cos(0.017*co)*d
+16.37*sin(0.017*co)*cos(0.017*co));
[6,6]=10^2*(0.61*cos(0.017*co)^2*d-16.37*cos(0.017*co)^2+2.27*d+47.60).
```

Appendix B

Because there is a significant difference between ND MUT and HFD MUT (1.78±0.02 mm vs. 1.62±0.03 mm, $p<0.01$), we adjusted the computed ε_{zz} for HFD MUT with respect to the ND MUT. For 3-point bending, we adjusted the stress σ_{zz} of the femur (f) with a correction factor (cf) equal to the ratio of the estimated stress due to bending at f's mid-shaft to that of reference femur (rf):

$$\mathrm{cf}=(\mathrm{Md}/\mathrm{I})_{\mathrm{rf}}/(\mathrm{Md}/\mathrm{I})_{\mathrm{f}} \quad (2)$$

where M is the moment of the force component, d is the distance between neutral axis and evaluation point, approximated by $(r_i+r_o)/2$ where r_i is the inner and r_o is the outer radius of the transverse section, and I is the second areal moments of inertia of the transverse section, $\pi(r_o^4-r_i^4)/4$. Because the bending moment is the same for all femora, equation (1) simplifies to:

$$\mathrm{cf}=(\mathrm{r_i}+\mathrm{r_o}/\mathrm{I})_{\mathrm{rf}}/(\mathrm{r_i}+\mathrm{r_o}/\mathrm{I})_{\mathrm{f}}. \quad (3)$$

For physiological loading, we adjusted the stress due to axial compression and the stress due to bending separately. We adjusted the stress due to axial compression by multiplying by a correction factor equal to the ratio of transverse section areas at mid-shaft. We used Eq. (2) to adjust the stress due to bending. In fact, we noted that the bending moments at mid-shaft were not significantly different in magnitude or direction among the groups ($p=0.06$). If θ denotes the angle between the neutral axis and the y-axis, $d=((r_i+r_o)/2)\sin(\theta)$ and Eq. (2) reduces to Eq. (3). The adjusted stress components for axial compression and bending were combined to yield the adjusted σ_{zz} that yielded the adjusted ε_{zz} by multiplication with compliance matrix. We dismissed adjustment of σ_{xy} that would alter ε_{zz} by less than 1%.

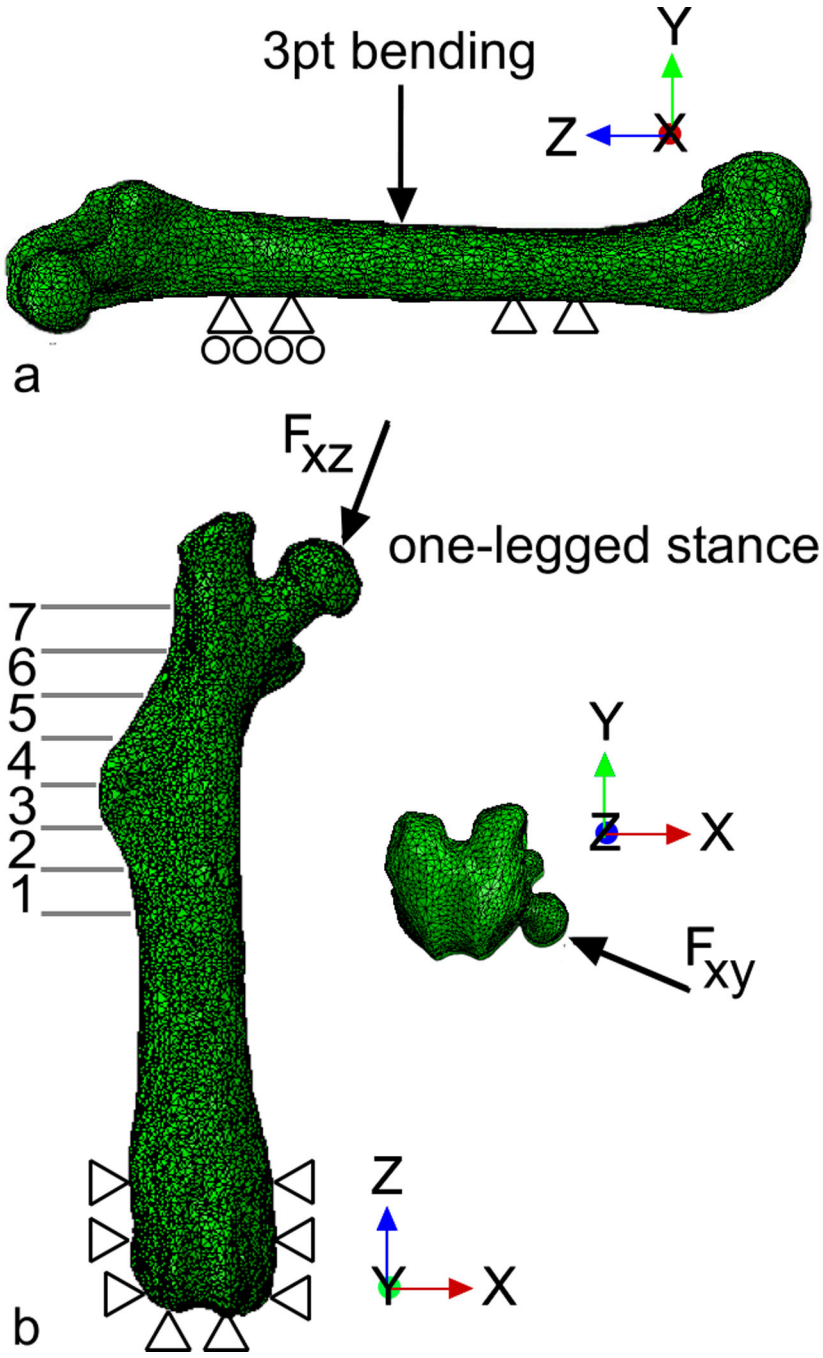

Figure 1.

mFE model of murine femur (a) under 3-point bending and (b) one-legged stance. 1mm bins 1 to 7 are indicated from mid-shaft to proximal femur in (b) and used for collection of data from microscopy investigations.

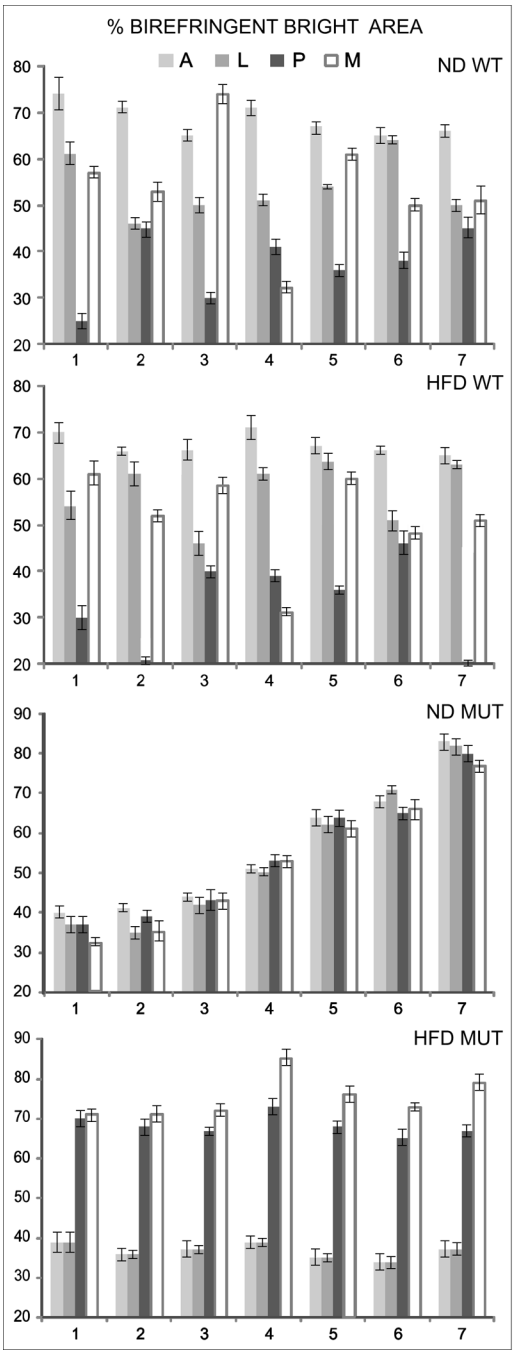

Figure 2.

% of bright area on longitudinal sections of murine femora. The percentages are shown per quadrant (A, anterior; L, lateral; P, posterior; M, medial) and per bin (numbered as 1 to 7, moving up from mid-shaft towards the proximal femur), per mouse group, averaged over the femora of the 4 mice in the group. The data of individual femora follow the trend of the averaged data.

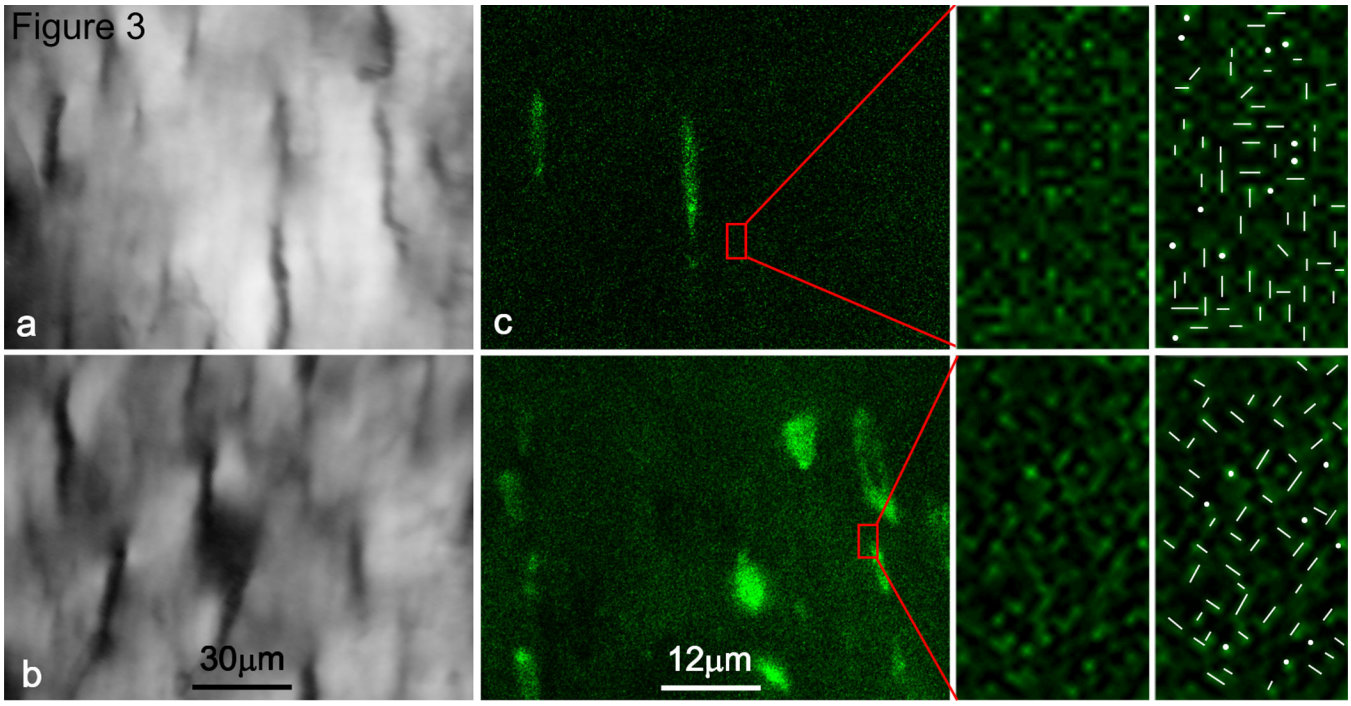

Figure 3.

Birefringent signal by CPL and fluorescent signal by confocal microscopy. We show examples of regions with specific percentages of bright areas: (a) 70% of bright area, occurring e.g. at the anterior quadrant of WT; and (b) 40% of bright area, e.g. at anterior mid-shaft of ND MUT and at anterior of HFD MUT. Confocal microscopy shows matrix and osteocyte lacunae of (c) ND WT and (d) HFD MUT. In enlargements, different collagen orientation patterns are emphasized with white markings.

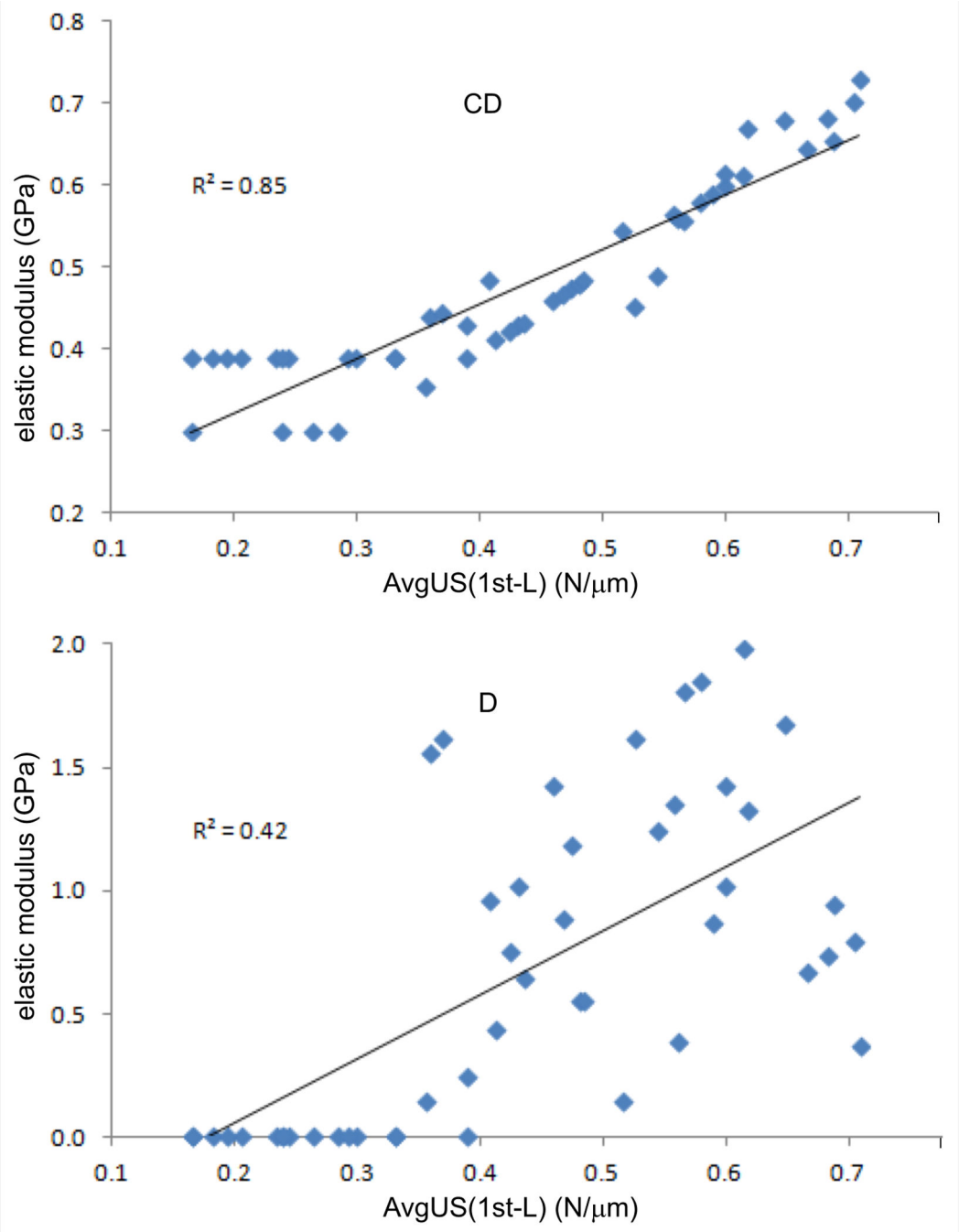

Figure 4.

Correlation of microindentation parameter Avg US (1st-L) with elastic modulus in anterior-posterior direction. The correlation was stronger for (a) collagen-density (CD) models than (b) density-only (D) models of 3 femora per group. The p-value of the r^2 were significant, $p<0.01$.

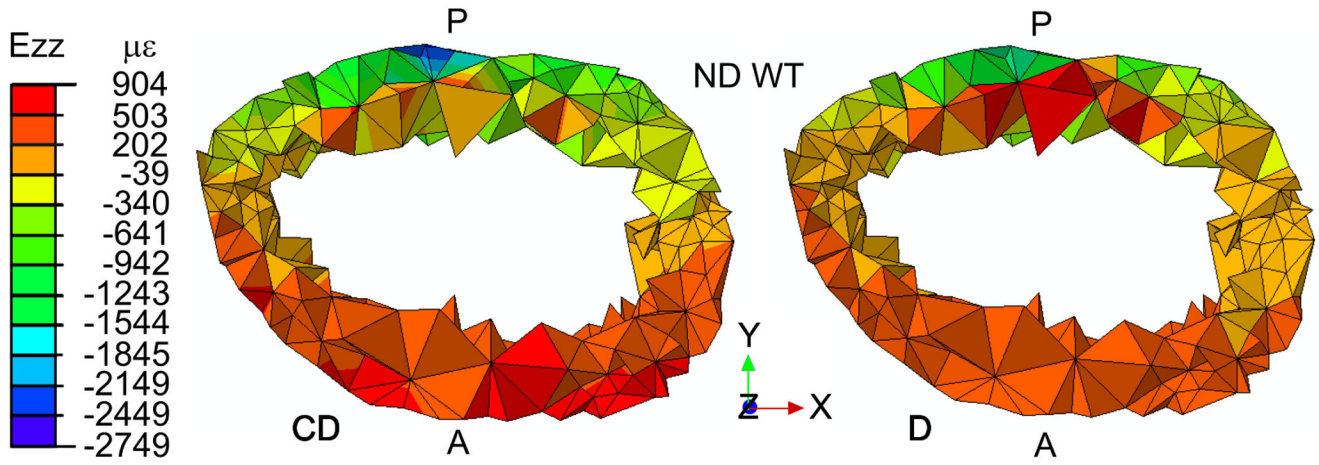

Figure 5.

Comparison of distributions of ε_{zz} at cortical mid-shaft between collagen-density (CD) and density-only (D) models. For 3-point bending, ε_{zz} was larger for CD than D at the anterior quadrant of ND WT (488±58 με vs. 301±26 με; Table I).

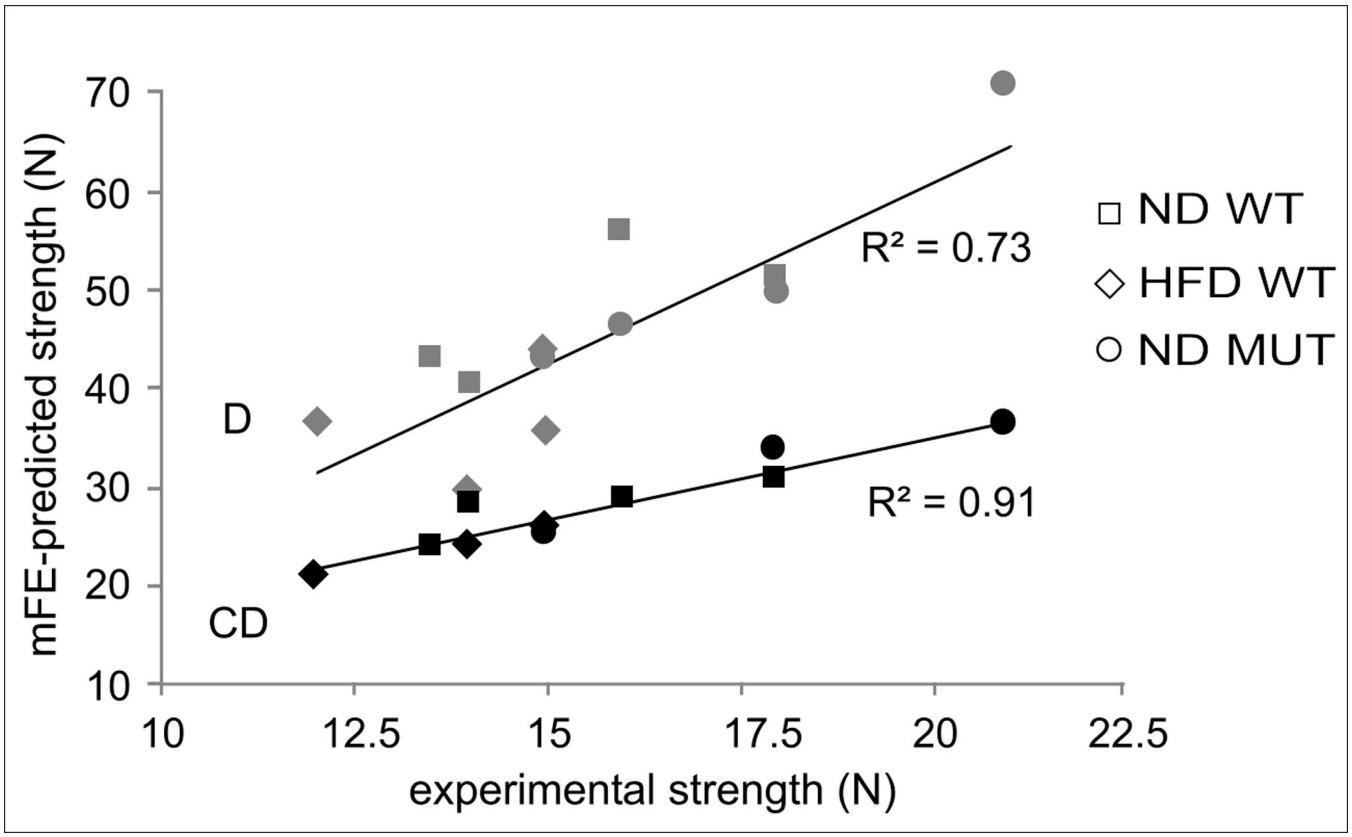

Figure 6.

Comparisons of distributions of ε_{zz} at cortical mid-shaft among collagen-density models. For one-legged stance, the absolute value of ε_{zz} was larger for (a) HFD WT than (b) HFD MUT at the anterior (336±56 με vs. 44±18 με; Table II, #2) and the posterior quadrant (977±72 με vs. 393±30 με; Table II, #4). The absolute value of ε_{zz} was larger for (a) HFD WT than (c) ND MUT at the posterior quadrant (977±72 με vs. 585±51 με; Table II, #4).

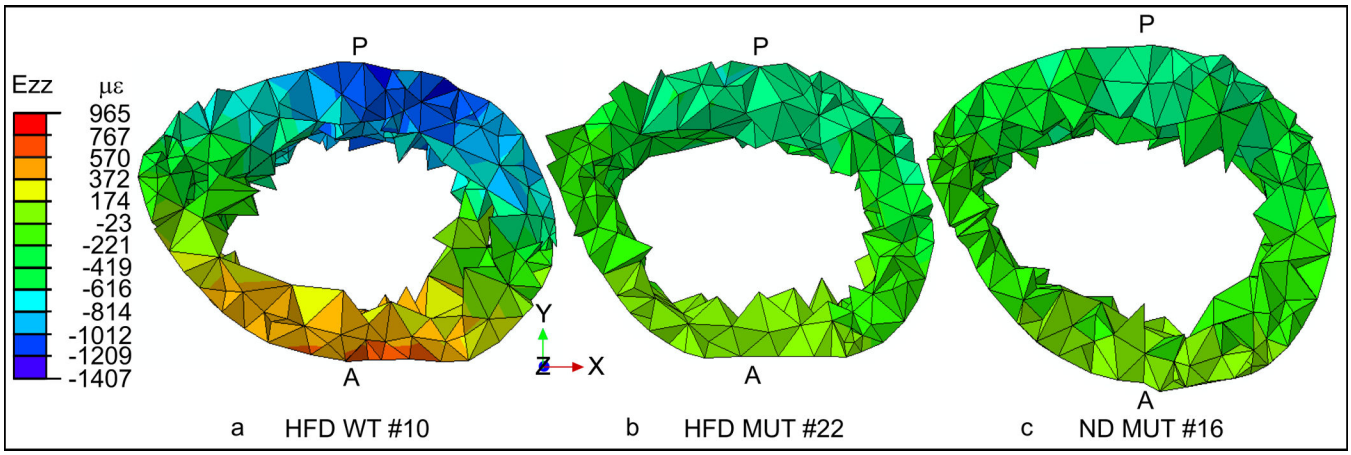

Figure 7.

Correlations between experimental bone strength and mFE-predicted strength for 3-point bending. The correlations were computed for ND WT, HFD WT and ND MUT at the anterior quadrant, for which ε_{zz} significantly differed between collagen-density (CD) models and density-only (D) models (Table I). The p-values of the r^2 were significant, $p<10^{-3}$.

Table I

Percentages of prevalent collagen orientation along the femoral shaft.

Group	Quadrant	Bin 1	Bin 2	Bin 3	Bin 4	Bin 5	Bin 6	Bin 7
ND WT	anterior	**48**	**47**	**43**	**47**	**44**	**43**	**44**
	lateral	44	49	48	47	46	50	48
	posterior	55	49	53	50	52	51	49
	medial	45	47	45	53	44	48	47
HFD WT	anterior	**46**	**43**	**44**	**47**	**44**	**44**	**43**
	lateral	46	44	49	44	43	47	44
	posterior	53	56	50	51	52	49	56
	medial	44	47	45	53	45	49	47
ND MUT	anterior	50	50	49	47	43	**45**	**54**
	lateral	51	52	50	48	44	**47**	**53**
	posterior	51	51	50	47	43	**43**	**52**
	medial	53	52	50	47	44	**44**	**50**
HFD MUT	anterior	51	52	51	51	52	52	51
	lateral	45	48	48	50	44	48	50
	posterior	**46**	**45**	**44**	**48**	**45**	**43**	**44**
	medial	47	**47**	**47**	**55**	**50**	**48**	**51**

The data is presented as mean percentages over the 4 mice of each group without standard errors in order to visualize differences in orientation patterns among groups. The bolded entries represent percentages in the longitudinal orientations of collagen (0°±22.5°) measured with respect to the longitudinal axis of the femur. The non-bolded entries are percentages in the oblique orientation of collagen, acute (45°±22.5°) and obtuse (135°±22.5°). The standard error varies up to 4%.

Table II

Pairwise comparison of strain component ε_{zz} (expressed in microstrain units) along the longitudinal (z) axis at mid-shaft, between collagen-density (CD) models and density-only (D) models of each mouse group.

Group	Quadrant	3-point bending			1-legged stance		
		CD	D	p	CD	D	p
ND WT	anterior	488 ± 58	301 ± 26	**0.009**	194 ± 40	95 ± 24	**0.044**
	posterior	−348 ± 299	−178 ± 216	0.648	−660 ± 61	−422 ± 34	**0.002**
HFD WT	anterior	507 ± 61	330 ± 44	**0.029**	336 ± 56	226 ± 33	0.105
	posterior	−340 ± 267	−158 ± 308	0.658	−977 ± 72	−722 ± 30	**0.004**
ND MUT	anterior	395 ± 49	262 ± 25	**0.029**	173 ± 39	105 ± 28	0.167
	posterior	−202 ± 195	−43 ± 242	0.611	−585 ± 51	−464 ± 24	**0.043**
HFD MUT	anterior	480 ± 50 *328 ± 34*	434 ± 27 *300 ± 19*	0.425 *0.481*	83 ± 22 *44 ± 18*	78 ± 22 *40 ± 22*	0.873 *0.872*
	posterior	−266 ± 296 *−78 ± 233*	−221 ± 331 *−68 ± 253*	0.918 *0.762*	−516 ± 35 −393 ± 30	−539 ± 25 −451 ± 22	0.585 *0.135*

We show ε_{zz} (mean ± standard error) and p-value (bolded if significant as less than 0.05), at each of anterior and posterior quadrant of the transverse section at mid-shaft, for each loading condition. Because the diameters of the transverse section at mid-shaft are smaller in HFD MUT than ND MUT, the adjusted ε_{zz} of HFD MUT is smaller than the original ε_{zz}. Adjusted strains and relative p-values are entered in italics.

Table III

Significant differences of strain ε_{zz} (expressed in microstrain units) among mouse groups.

Loading	Quadrant	Significant differences						p	#
3-point bending	anterior	D	ND WT:	301 ± 26	vs.	HFD MUT:	434 ± 27	0.002	1
			ND MUT:	262 ± 25	vs.	HFD MUT:	434 ± 27	0.001	
one-legged stance	anterior	CD	HFD WT:	336 ± 56	vs.	HFD MUT:	83 ± 22 *44 ± 18*	$5 * 10^{-4}$ *10^{-5}*	2
		D	HFD WT:	226 ± 33	vs.	ND WT:	95 ± 24	0.003	
					vs.	HFD MUT:	78 ± 22 *40 ± 19*	0.001 *10^{-4}*	
	posterior	CD	ND WT	−660 ± 61	vs.	HFD MUT:	*−393 ± 30*	*0.001*	3
			ND MUT	*−585 ± 51*	vs.	HFD MUT:	*−393 ± 30*	*0.003*	
			HFD WT:	−977 ± 72	vs.	ND MUT:	−585 ± 51	10^{-4}	4
					vs.	ND WT:	−660 ± 61	0.002	
					vs.	HFD MUT:	−516 ± 35 *−393 ± 30*	10^{-5} *$3 * 10^{-7}$*	
		D	HFD WT:	−722 ± 30	vs.	ND MUT:	−464 ± 24	$2 * 10^{-7}$	5
					vs.	ND WT:	−422 ± 34	$2 * 10^{-7}$	
					vs.	HFD MUT:	−539 ± 25 *−451 ± 22*	$5 * 10^{-5}$ *10^{-7}*	

We show differences for each loading condition, at each of anterior and posterior quadrant of mid-shaft, for collagen-density (CD) models and for density-only (D) models. Strains of HFD MUT, adjusted for smaller diameters at mid-shaft, and relative p-values are shown in italics. Because we compared 4 groups, we used Bonferroni's coefficient m=6, the p-values are considered significant if smaller than 0.0083. Note that the comparisons for 3-point bending (#1) lose their significance after strain adjustment of HFD MUT due to its smaller mid-shaft diameters than ND MUT (Table III).